In-situ synthesis of bimetallic phosphide with carbon tubes as an active electrocatalyst for oxygen evolution reaction

Jian Wang[a], Francesco Ciucci[a,b,*]

[a] Department of Mechanical and Aerospace Engineering, The Hong Kong University of Science and Technology, Hong Kong, China
[b] Department of Chemical and Biological Engineering, The Hong Kong University of Science and Technology, Hong Kong, China

A R T I C L E   I N F O

A B S T R A C T

Transition metal phosphides (TMPs) are attracting increasing interest as promising electrocatalysts for the oxygen evolution reaction (OER). Coupling TMPs with carbon materials can increase OER activity by improving the dispersion of active sites and introducing more OER-active species. However, the overwhelming majority of previous works have used either ex-situ methods to prepare TMPs@carbon hybrids or have obtained TMPs@ disordered carbons. Here, we report an in-situ synthesized TMPs coupled with carbon tubes as an active OER catalyst. Bimetallic NiFe phosphide ($Ni_{2-x}Fe_xP$) coupled with N/P co-doped carbon tubes (NPC), i.e., $Ni_{2-x}Fe_xP@$ NPC, is prepared by pyrolyzing phytic acid sodium salt hydrate, melamine, and transition metal nitrate. Bimetallic NiFeP@NPC is found more active in catalyzing OER compared to monometallic $Ni_2P@NPC$ and $Fe_2P@NPC$, metal-free NPC, and NiFeP@P-doped disordered carbon (NiFeP@PC). Its high performance is attributed to the unique tubular structure of its carbon material and the addition of a second metal into binary TMPs, contributing to a larger electrochemical active surface area and faster charge transfer kinetics. Moreover, NiFeP@NPC exceeds the benchmark RuO_2 in terms of the OER activity, and it exhibits little activity degradation in both accelerated aging and chronopotentiometric tests, demonstrating a great promise as a high-performance OER electrocatalyst.

1. Introduction

Oxygen evolution reaction (OER) is critical for many sustainable energy conversion and storage technologies including regenerative fuel cells, water-splitting electrolyzers, and metal-air batteries [1–4]. However, the sluggishness of OER, which involves multi-electron transfer steps, results in substantial internal losses and reduced performance. The state-of-the-art OER electrocatalysts are based on precious metals such as Ru and Ir, which suffer many significant issues including high cost, limited availability, and poor operational durability. These factors ultimately hinder the large-scale application of the above-mentioned sustainable energy technologies.

Various non-precious OER electrocatalysts including, but not limited to, transition metal oxides/hydroxides [5,6], chalcogenides [7,8], and metal-free carbons [9,10] have been investigated extensively. Among them, transition metal phosphides (TMPs) are gaining significant interest from researchers worldwide because of their promising activity and abundance in the earth's crust [11–14]. Various strategies have been reported to further improve the OER activity of TMPs, such as elemental doping/alloying [15], tuning porosity [11,16], and

manufacture of nanostructures [17]. For example, Li et al. found that moderate O doping into the TMPs could enhance their electrical conductivity and elongate the M–P bonds, facilitating the electron transfer and improving the OER activity [15]. In another work, Lin and co-authors used a hard template method with KIT-6, a mesoporous silica material, to prepare highly ordered mesoporous CoP and NiP nanoparticles [11]. Thanks to the unique porous structure, the transfer of mass and electrons were facilitated and, in turn, OER kinetic rates improved [11]. In contrast to binary TMPs such as Ni_2P, introducing another metal to form ternary TMPs with a more beneficial electronic structure and bond coordination can enhance the OER activity [18]. Various bimetallic phosphides such as CoMnP [12], $Fe_{2-x}Mn_xP$ [19], $(Co_xFe_{1-x})_2P$ [20], and Co_xNi_yP [21], have been reported to improve the OER activity over their monometallic phosphide counterparts.

Even though TMP-based OER electrocatalysts have advanced over the past few years, further improving the OER catalytic performance is limited by their poor electronic conductivity, and an insufficient number of active sites [22,23]. Coupling TMPs with carbon materials could resolve these challenges. In fact, carbon supports have been reported to improve not only the conductivity but also prevent TMPs from

agglomeration, enhancing the dispersion of active sites [24–27]. Also, carbons can provide additional active sites for OER [28]. To obtain TMPs/carbon hybrids, previous works have generally resorted to two approaches. One method is to prepare carbons and TMPs separately, and then physically mix the two materials [29–32]. This process, however, does not favor an intimate contact, and TMP nanoparticles are easily separated from the carbon due to the interaction of generated gas during OER [33]. Alternatively, mating carbon and TMP via in-situ carbonization and phosphidization improves the electrical contact and the overall coupling. However, for many previous works, the carbons obtained by in-situ methods are usually disordered [34–38]. Disordered carbon materials are not favorable for a high catalytic performance because of their reduced electronic conductivity and lowered corrosion tolerance [39].

A number of works have demonstrated that bimetals contribute to a higher degree of graphitization and reduced disorder in prepared carbons, in comparison to their monometallic counterparts [40–42]. In a previously published article, we added different bimetals including NiFe, FeCo, FeMn, CoNi, MnCo, and NiMn, respectively, during the preparation of N-doped carbon. We found that NiFe produces the largest, most robust, and least disordered carbon tubes, leading to the highest OER activity [43]. Carbon tubes are characterized by relatively high electronic conductivities and large surface areas, and can be combined with TMPs to improve the catalytic performance [29–32]. However, to the best of our knowledge, there is limited number of works reporting the in-situ preparation of carbon tubes and phosphidization of transition metal to achieve TMPs/carbon hybrids [44].

In this work, we synthesized nickel iron phosphide in-situ together with N/P co-doped carbon tubes, i.e., NiFeP@NPC as an effective OER electrocatalyst. By adjusting the Ni to Fe molar ratios, we were able to get different $Ni_{2-x}Fe_xP@NPC$ (x = 0, 0.5, 1, 1.5, and 2). $Ni_{2-x}Fe_xP@NPC$ was prepared by the pyrolysis of a mixture containing phytic acid sodium salt hydrate, melamine, and transition metal salts. During the process, in-situ carbonization and phosphidization were achieved: the transition metal salts catalyzed the graphitization of melamine producing carbon tubes [45], while the six phosphate groups in phytic acid sodium salt provided additional P sources doped into the carbon [15,46], and also cross-linked the metal ions to generate TMPs [15,46]. Combining Fe and Ni contributed to less disordered carbons with reduced I_D/I_G ratio in the Raman spectra, and also induced a chemical shift of Ni 2p and P 2p XPS spectrum, indicating an electronic structure change. NiFeP@NPC is found much more OER-active than monometallic $Ni_2P@NPC$ and $Fe_2P@NPC$, metal-free NPC, NiFeP@P-doped disordered carbon (NiFeP@PC), and even RuO_2, a commercial catalyst. Also, this NiFeP@NPC exhibits little activity degradation during accelerated aging and chronopotentiometric tests.

2. Materials and methods

2.1. Sample preparation

SBA-15 which was used as the hard template to fabricate pores was prepared following the previous work [47]. First, quantitative amounts of tetraethoxysilane (TEOS, > 98%, Sigma Aldrich), P123 (Sigma Aldrich), hydrochloric acid (37 wt.%, analytical reagent grade, Sigma Aldrich), and water were mixed, stirred, and hydrothermally treated. Then, the product was filtered, dried, and finally calcined at 550 °C to obtain the SBA-15 powder.

The precursors, melamine ($C_3H_6N_6$, analytical reagent grade, Sinopharm Chemical Reagent Co., Ltd), iron (III) nitrate nonahydrate ($Fe(NO_3)_3 \cdot 9H_2O$, analytical reagent grade, Sigma Aldrich), nickel (II) nitrate hexahydrate ($Ni(NO_3)_2 \cdot 6H_2O$, analytical reagent grade, Sigma Aldrich), and phytic acid sodium salt hydrate ($C_6H_6Na_{12}O_{24}P_6 \cdot xH_2O$, > 98%, Hefei Bomei Biotechnology. Co., Ltd), were used as received without purification. For each batch of $Ni_{2-x}Fe_xP@NPC$, we used 0.5 g of SBA-15 together with 8.40 g of melamine,

and 6.16 g of phytic acid sodium salt hydrate, which served as source of C, N, and P. 0.002 mol of transition metal salts were added, and by adjusting the Ni to Fe molar ratios, we were able to prepare $Fe_2P@NPC$ (0 : 2), $Ni_{1.5}Fe_{0.5}P@NPC$ (3 : 1), NiFeP@NPC (1 : 1), $Ni_{0.5}Fe_{1.5}P@NPC$ (1:3), and $Ni_2P@NPC$ (2 : 0). The reagents were carefully weighed, dissolved in ethanol (Sigma Aldrich), and finally sonicated for 2 h. The obtained slurry was subsequently dried at 60 °C to remove ethanol. Following that, the dried aggregate was ground, put into a ceramic crucible, and annealed in a tube furnace (GSL 1100X, MTI). The annealing was performed at 800 °C for 2 h in N_2 (> 99.99%) with a gas flow rate of 50 sccm. The ramping rate for heating and cooling was set at 5 °C min^{-1}. The obtained product was first dissolved in 10 M NaOH (Sigma Aldrich) under stirring at 120 °C for 24 h to remove the SBA-15 template, and then washed with 0.5 M HCl, ethanol and deionized water to eliminate unreacted reactants and unstable species [22]. Subsequently, the material was vacuum dried at 60 °C for 1 h. We followed a nearly identical recipe to make 1) NPC by pyrolyzing the reactants without transition metal salts; 2) NiFeP@PC by not using melamine [46].

2.2. Basic characterizations

An Empyrean PANalytical diffractometer was used to perform the powder X-ray diffraction (XRD) scans in the range of 2θ = 10 - 60° with steps of 0.02°. Cu K-alpha radiation (λ = 1.5406 Å, 40 kV, 40 mA) was used as the incident X-ray source. Raman spectra were scanned using a Renishaw inVia Raman microscope to evaluate the degree of disorder in as-prepared carbons. The chemical compositions near the surface were examined by X-ray photoelectron spectroscopy (XPS, PHI5600 equipped with a monochromatic Al-source X-ray). The Brunauer-Emmett-Teller (BET) specific surface areas were obtained from the N_2 adsorption and desorption isotherms measured at 77 K using a Beckman Coulter SA3100 analyzer. Scanning electron microscopy (SEM, JEOL, 6390) and transmission electron microscopy (TEM, JEM-2010 F) micrographs were taken to assess the micro- and nano-structures of the samples we prepared.

2.3. Electrochemical test

The OER electrochemical characteristics were tested in ambient temperature with a rotating ring-disk electrode (RRDE-3A, BAS Inc.) setup based on a three-electrode cell configuration. The rotating speed is 2000 rpm. Catalyst-modified glassy carbon (GC, 4 mm in diameter), Pt wire, and Ag/AgCl (filled with 3 M NaCl) were used as the working, counter, and reference electrodes, respectively. An ALS2325E potentiostat was employed to control the polarization potential. For all the samples, the catalyst ink was prepared by drop-casting. In short, 10 mg of each sample was dispersed in 2 mL of mixed ethanol (1.9 ml) -5 wt% Nafion (0.1 mL) solution. The suspension was then sonicated for 1 h to reduce agglomeration. Finally, 10 μL of the homogenously dispersed catalyst ink was loaded onto the polished glassy carbon electrode surface with a ~0.4 mg cm$_{disk}^{-2}$ loading. Before each test, the electrolyte (1.0 M KOH) was purged with O_2 for more than 30 min. We kept the gas flowing during the experiments. Linear sweep voltammetry (LSV) responses were recorded from 0 to 1 V vs. Ag/AgCl for OER with a potential scan rate of 5 mV s^{-1}. Unless specified, the potentials were corrected by subtracting the potential loss caused by the Ohmic resistance of the electrolyte (~31 Ω).

The electrochemical active surface area (ECSA) was evaluated using cyclic voltammograms (CVs), which were scanned between 1.1 and 1.2 V vs. RHE [43,48,49]. In that potential range, the Faradaic current is negligible and the detected current i results from the double-layer capacitive charging [43,48,49]. Specifically, the current i depends linearly on the electrochemical double-layer capacitance C_{DL} following:

$$i = C_{DL}\dot{v}$$

where $\dot{v}$ is the potential scan rate (we used 0.02 V s^{-1}, 0.05 V s^{-1}, 0.1 V s^{-1}, and 0.2 V s^{-1}). Half of the anodic and cathodic current difference, i.e., $\Delta i/2 = (i_a - i_C)/2$, centered in the middle of the potential scanning range (1.15 V vs. RHE), was used to calculate the capacitance, the value of which is expected to be linearly proportional to the ECSA [43,48,49].

To obtain the charge transfer resistance during OER, we carried out electrochemical impedance spectroscopy (EIS) using a VSP (BioLogic) electrochemical workstation in the frequency range from 0.1 Hz to 100 kHz. During the EIS tests, AC voltage amplitude was set at 10 mV and the potential of the working electrode at 1.7 V vs. RHE [2].

3. Results and discussion

Ni$_{2-x}$Fe$_x$P@NPC was prepared by the pyrolysis of a mixture including melamine, phytic acid sodium salt hydrate, nickel and iron nitrate salt. In contrast to phytic acid, phytic acid sodium salt hydrate is solid and therefore can be more easily handled. Mesoporous silica SBA-15 (see the microstructure in **Fig. S1** in the supporting information) was added during the pyrolysis to fabricate pores [50]. By varying the Ni to Fe molar ratio, we made Ni$_{0.5}$Fe$_{1.5}$P@NPC, NiFeP@NPC, Ni$_{1.5}$Fe$_{0.5}$P@NPC, Ni$_2$P@NPC, and Fe$_2$P@NPC. The preparation method is schematically illustrated in Scheme 1 and detailed in the experimental part of this article. After the dissolution and ultrasonic treatments of precursors, the complex composed of phytic acid sodium salt, melamine, and the transition metal ions, formed. In this complex, melamine and phytic acid sodium salt can serve as C sources [43,46,51–53], and melamine provides extra N while phytic acid sodium salt provides additional P. Many previous reports have demonstrated that transition metal salts such as Fe, Co, and Ni nitride or acetate, can improve the graphitization degree of melamine to generate carbon tubes [43,51–53]. During the pyrolysis process, the complex was decomposed and carbonized to produce N/P co-doped carbon tubes, where the phytic acid sodium salt and melamine provides P and N, respectively [54]. Meanwhile, six phosphate groups in phytic acid sodium salt and the cross-linked transition metal ions were transformed into TMPs [13,15,46]. Subsequently, we washed out the SBA-15 template. We also synthesized NPC following the same preparation method illustrated for NiFeP@NPC with the sole difference that we did not add transition metal salts [37]. However, we were not able to synthesize NiFeP alone by pyrolyzing phytic acid sodium salt and transition metal salt without melamine, since carbonizing phytic acid sodium salt can lead to P-doped disordered carbon (PC) [46]. The sample prepared by the pyrolysis of phytic acid sodium salt hydrate, nickel, and iron salt without melamine is denoted as NiFeP@PC. Melamine appears to be necessary for the formation of the carbon tubes [43,51–53]. In order to investigate the effect of the transition metal and the pyrolysis temperature on the prepared samples, we increased the mass of added metal salts by a factor of 10 (this compound is denoted as NiFeP10@NPC) and we also prepared NiFeP@NPC at 800, 900, and 1000 °C.

We examined the structure of the materials by XRD. From Fig. 1(**a**), for Ni$_2$P@NPC, the distinct reflections located at around 40.7°, 44.6°, 47.3°, 54.2°, and 54.9° can be attributed to the (111), (201), (210),

(300), and (211) crystal plane of the hexagonal Ni$_2$P phase (P-62 m, ICOD 03-065-1989). Varying the Ni to Fe molar ratio fails to change the XRD patterns significantly. It is clear that Ni$_{0.5}$Fe$_{1.5}$P@NPC and NiFeP@NPC share similar diffraction characteristics as Ni$_2$P@NPC. In addition to the diffraction peaks attributed to TMPs, a peak located at around 26.4° for NiFeP@NPC is also observed, which is indexed to the (002) plane of graphitic carbon (ICOD 00-008-0415). Such a characteristic peak is much narrower for Ni$_2$P@NPC and NiFeP@NPC in contrary to that of NPC, suggesting their enlarged crystallites and reduced disorder in carbons according to the Scherrer equation.

We also took the Raman spectra shown in Fig. 1(**b**). Two distinct characteristic peaks located at around 1582, 1352 cm^{-1} are detected and are assigned to the G and D carbon band, respectively [55]. The G band results from the bond-stretching motion of sp^2 C, while the D band is related with defects present in carbon [55]. By comparison, metal-free NPC (I$_D$/I$_G$ = 1.38) and monometallic Ni$_2$P@NPC (I$_D$/I$_G$ = 1.04), are characterized by a larger I$_D$/I$_G$ ratio than bimetallic NiFeP@NPC (I$_D$/I$_G$ = 0.92), suggesting a decreased carbon disorder in NiFeP@NPC. This finding agrees well with previous reports that transition metal salts can catalyze the graphitization of carbon, and bimetal-based catalysts contribute more to a higher degree of graphitization in comparison to monometallic counterparts [41,43,56]. We should also note that NiFeP@NPC (I$_D$/I$_G$ = 0.92) is characterized by a reduced I$_D$/I$_G$ ratio in comparison to NiFeP@PC (I$_D$/I$_G$ = 1.21), which will be discussed later with TEM photos.

As shown in Fig. 1(**c**), which reports the N$_2$ adsorption/desorption isotherm curves, NiFeP@NPC (154.9 m^2 g^{-1}) has a similar BET surface area (S$_{BET}$) as Ni$_2$P@NPC (148.7 m^2 g^{-1}). Increasing the added transition metal amount leads to a significant drop of the surface area (S$_{BET}$ of NiFeP10@NPC is only 62.4 m^2 g^{-1}). This decrease may be related with the agglomeration of transition metal phosphide nanoparticles in NiFeP10@NPC, which will be carefully clarified later. Moreover, if no SBA-15 as the template to porous structure is added during the synthesis, S$_{BET}$ of NiFeP@NPC is dramatically reduced (by ~89%) to only 17.2 m^2 g^{-1}, accompanied by significantly reduced OER activity (see **Fig. S5** in the Supporting information).

The XPS in Fig. 1(**d**) detects the presence of the target elements including C, N, P, Ni, and Fe for NiFeP@NPC, and O is also observed due to air exposure [11,57]. The elemental contents of Ni$_{0.5}$Fe$_{1.5}$P@NPC, NiFeP@NPC, Ni$_{1.5}$Fe$_{0.5}$P@NPC, Ni$_2$P@NPC, Fe$_2$P@NPC, NPC, and NiFeP@PC are shown in **Table S1**. From **Table S1**, about ~2.2 at.% of TMPs is left in Ni$_{2-x}$Fe$_x$P@NPC. C 1s (Fig. 1(**e**)) has four contributions including C–C/C = C (284.6 eV), C–N/C-P (285.3 eV), C–O (286.4 eV), and C = O (287.6 eV) [58]. The N 1s (Fig. 1(**f**)) can be deconvolved into 4 peaks centered at 398.7, 399.9, 401.3, and 403.0 eV, which are assigned to pyridinic N, pyrrolic N, graphitic N, and oxidized N, respectively [59]. P 1s (Fig. 1(**g**)) is divided into 4 peaks, among which the ones centered at 134.0 and 133.2 eV belong to P-O and P-C, respectively, and the peaks located at 130.5 and 129.5 eV are attributed to P-M 2p 1/2 and 2p 3/2 (M = Ni, Fe) [22,60]. Ni 2p contains two contributions including Ni-P (856.7 eV) and Ni-O (862.5 eV) [35], see Fig. 1(**h**). Similarly, Fe 2p (Fig. 1(**i**)) can also be deconvoluted into Fe-P
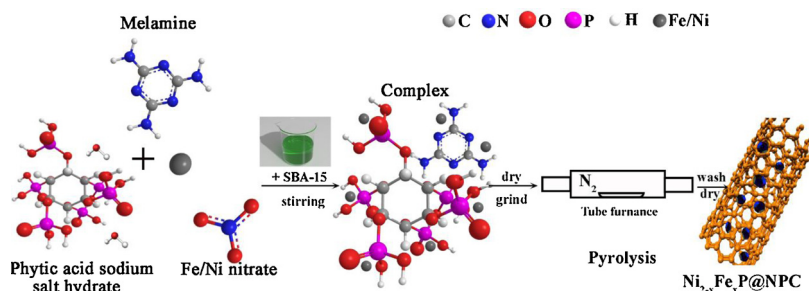
**Scheme 1.** Illustration of the synthesis of the TMPs coupled with carbon tubes.
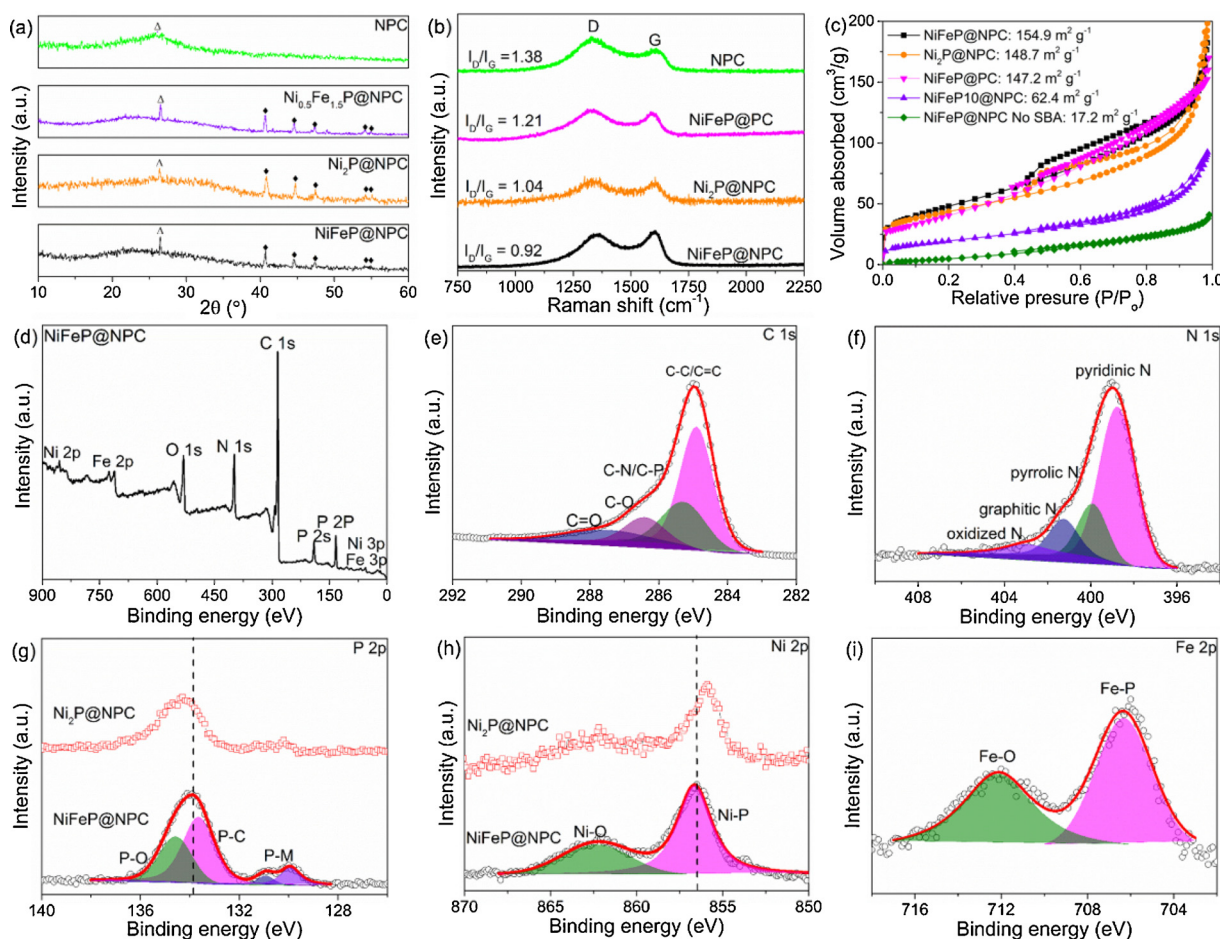
Fig. 1. Structural and compositional characterization of synthesized samples: (**a**) XRD, where the ◆ symbols indicate the peaks pertaining to $Ni_{2-x}Fe_xP$, while Δ represents the (002) plane of graphitic carbon; (**b**) Raman spectra; (**c**) N_2 adsorption-desorption isotherm curves with the corresponding BET surface areas; (**d**) XPS survey spectrum of NiFeP@NPC; XPS deconvolution for (**e**) C 1s; (**f**) N 1s; (**g**) P 2p; (**h**) Ni 2p; and (**i**) Fe 2p.

(706.5 eV) and Fe-O (712.3 eV) [22,60]. Those Ni-O/Fe-O moieties are attributed to the partial oxidation of transition metal on the surface of TMPs due to air exposure [22,35,60]. The XPS results above suggest that N and P have been doped into carbon, and NiFe phosphide is formed. In addition, we observed that the Ni 2p XPS spectrum in NiFeP@NPC positively shifted relative to Ni_2P@NPC, see Fig. 1(**h**), and the P 2p negatively shifted, as shown in Fig. 1(**g**). Such shifts of XPS spectrum have also been reported for other bimetallic TMPs such as CoFeP [16], suggesting a modified electronic configuration in the bimetallic TMPs after introducing the second metal.

From the SEM image of NiFeP@NPC in Fig. 2(**a**), tube-like carbon structures are observed. The energy-dispersive X-ray spectroscopy (EDX) in **Fig. S2** detect various elements including Ni, Fe, P, N, and C. The corresponding mapping in Fig. 2(**b**) shows that Ni, Fe, and parts of P are coupled together, implying that NiFe TMPs are formed. Atomic contents obtained from EDX determine the total amount of Ni and Fe to be ~2.5 at. %, consistent with XPS results. As shown by the TEM (see Fig. 2(**c**)), NiFeP@NPC displays a tube morphology [61]. From Fig. 2(**d**), a porous structure is observed for the carbon. A small nanoparticle is embedded in the carbon, as shown in Fig. 2(**e**). The magnified TEM image and corresponding fast Fourier transformation (FFT) determine the lattice space of the embedded nanoparticle to be 0.22 nm, which corresponds to the (111) plane of NiFeP, see **Fig. S3**. Upon closer observation from Fig. 2(**f**), graphitic ribbons are generally orderly distributed in NiFeP@NPC, and the FFT of the selected region can be indexed to the (002) plane of graphitic carbon, suggesting a certain degree of graphitization. This result agrees well with the relatively sharp XRD peak assigned to (002) plane of graphitic carbon in

Fig. 1(**a**). A tube-like morphology is also observed for $Ni_{0.5}Fe_{1.5}P$@NPC and Ni_2P@NPC, see **Fig. S4**(**a**) and (**b**). However, only disordered carbon is formed in the case of NPC and NiFeP@PC, see the TEM images and corresponding FFT in **Fig. S4**(**c**)–(**h**), and no specific morphology is detected, in good agreement with previous reports [37,46]. The much higher level of disorder in NiFeP@PC is consistent with its larger I_D/I_G ratio ($I_D/I_G = 1.21$) in comparison to that of NiFeP@NPC ($I_D/I_G = 0.92$) in the Raman spectrum, see Fig. 1(**b**). The tube-shaped structure of $Ni_{2-x}Fe_xP$@NPC is expected to provide a continuous pathway that improves the transport of reactants and the ion exchange between the catalyst surface and the inner layers [43,56,62].

The catalytic performance of the samples was evaluated in 1.0 M KOH solution, and we should note that all reported potentials have been corrected to be against the reversible hydrogen electrode (RHE), see the details in **Fig. S6**. In addition, the potential loss caused by the Ohmic resistance of the electrolyte has been subtracted, see the comparison between Fig. 3(**a**) and **Fig. S7**. From Fig. 3(**a**), the onset overpotentials have been reduced, and the current densities have been dramatically enhanced for Ni_2P@NPC, Fe_2P@NPC, NiFeP@PC, $Ni_{0.5}Fe_{1.5}P$@NPC, $Ni_{1.5}Fe_{0.5}P$@NPC, and NiFeP@NPC in comparison to NPC. Furthermore, washing NiFeP@NPC in 1.0 M H_2SO_4 at 80 °C for 24 h to leach NiFeP [22] leads to a lowered OER activity (**see Fig. S8**). Both results support the finding that $Ni_{2-x}Fe_xP$ plays a positive role in enhancing the OER. Also, bimetallic NiFeP@NPC (= 0.35 V), $Ni_{0.5}Fe_{1.5}P$@NPC (η= 0.39 V), and $Ni_{1.5}Fe_{0.5}P$@NPC (η= 0.41 V) have higher OER activities with reduced overpotential (η) to deliver 10 mA cm^{-2}, in comparison to monometallic Ni_2P@NPC (η= 0.44 V), Fe_2P@NPC (η= 0.51 V), and NiFeP@PC (η= 0.46 V). It is worth noting that the
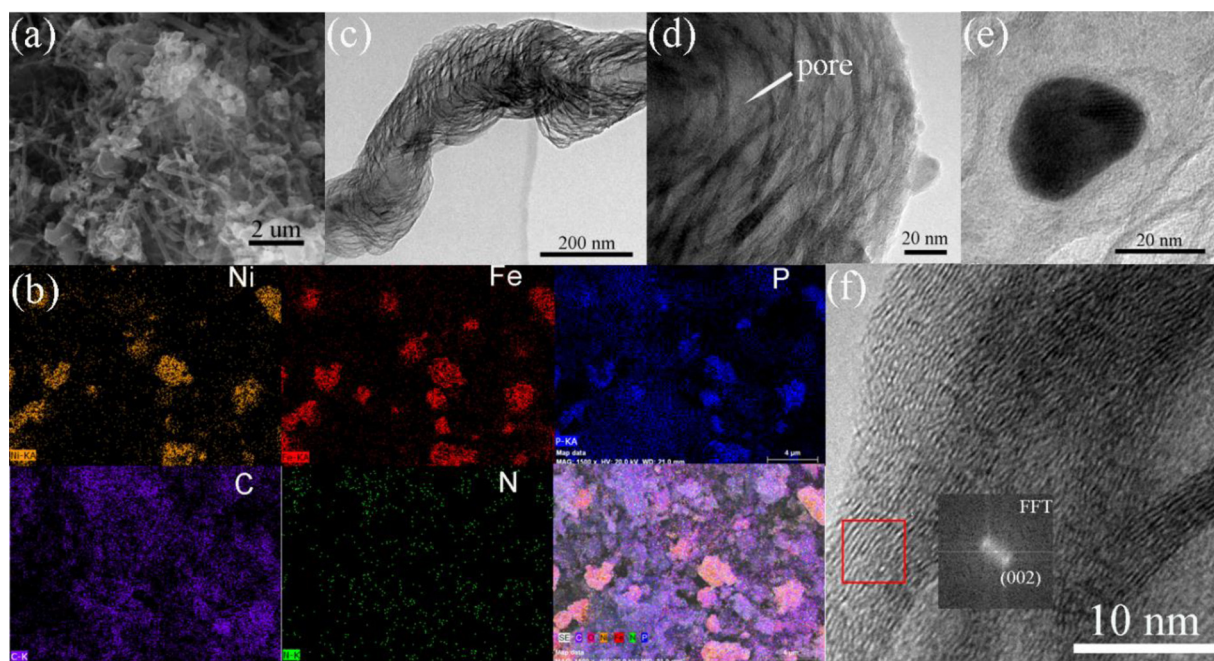
Fig. 2. Micro- and nano-structural characterization of NiFeP@NPC: (**a**) SEM; (**b**) Ni, Fe, P, C, N EDX mapping where the scale bar is 4 um; (**c**), (**d**), (**e**) and (**f**) TEM micrographs taken at different magnifications. The inset in (**f**) is the FFT of the region highlighted by the red line. (For interpretation of the references to colour in this figure legend, the reader is referred to the web version of this article).

OER activity of NiFeP@NPC even exceeds that of the benchmark catalyst, RuO_2. This finding is also confirmed by its smaller Tafel slope (78 mV dec^{-1}) than that of RuO_2 (87 mV dec^{-1}), see Fig. 3(**b**). A smaller Tafel slope endows the catalyst with better OER catalytic kinetics without requiring substantially increased overpotentials. In addition, the OER activity of NiFeP@NPC is comparable to, or even better than that of many state-of-the-art OER electrocatalysts, see **Table S2**.

The origin of the high anodic current measured in NiFeP@NPC was investigated using an RRDE setup, see the inset in Fig. 3(**c**). To monitor

the generation of H_2O_2, the Pt ring was kept at a potential high enough, i.e., 1.5 V vs. RHE, to oxidize H_2O_2 [63]. Conversely, to reduce the oxygen evolved from the working electrode, the Pt ring was held at 0.4 V vs. RHE. The OER Faradaic efficiency is estimated with the formula of $I_{ring}/(I_{disk} \times N)$, where I_{ring}, and I_{disk} represent ring and disk current, respectively, and N is the collection efficiency of the Pt ring [63]. From Fig. 3(**c**), the oxygen reduction reaction (ORR) current on the ring increases with the OER current on the disk, leading to a Faradaic efficiency greater than 92%. Moreover, from the same plot, no
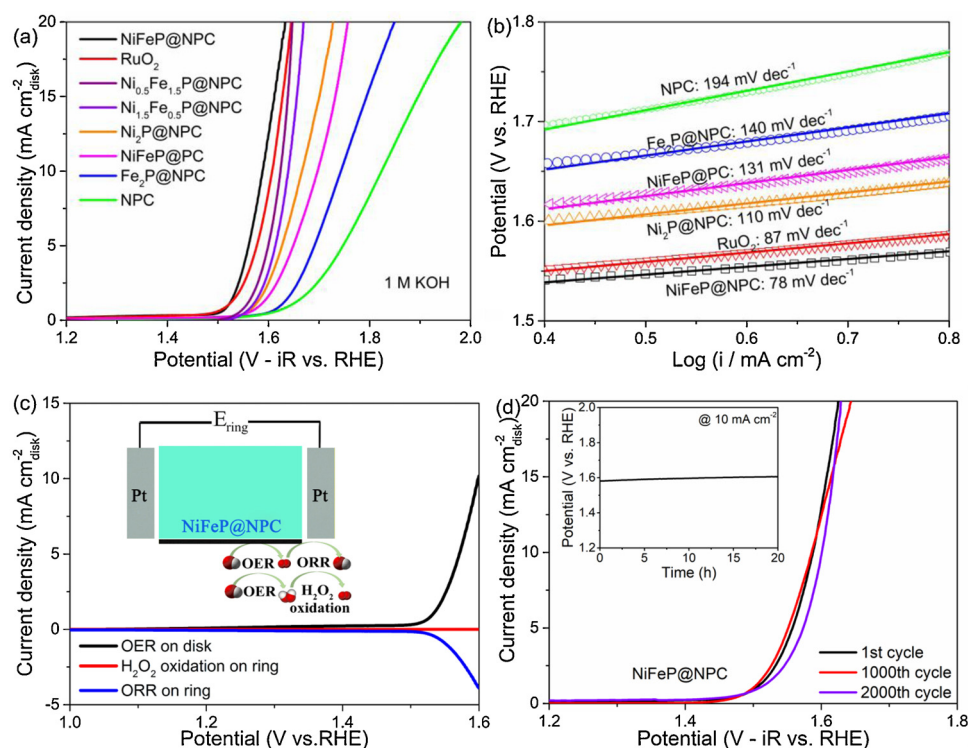
Fig. 3. OER performance evaluation: (**a**) polarization curves; (**b**) Tafel plots; (**c**) detecting ORR and potential H_2O_2 on the Pt ring caused by OER on the disk for NiFeP@NPC through a RRDE setup (schemed in the inset); (**d**) NiFeP@NPC LSV curves before and after 1000 cycles. The inset shows the chronopotentiometric test response at 10 mA cm^{-2}.

apparent H_2O_2 oxidation current is detected. These findings imply that the detected high OER current density for NiFeP@NPC is mainly attributed to the efficient $4e^-$ pathway ($4OH^- \rightarrow O_2 + 2H_2O + 4e^-$) instead of the undesirable 2e- peroxide formation ($2OH^- \rightarrow H_2O_2 + 2e^-$) or other side reactions such as carbon oxidation [63,64]. The OER stability of NiFeP@NPC was investigated by both accelerated aging and chronopotentiometric tests. The CV scans were recorded for 2000 cycles over the OER potential region, see **Fig. S9**. As apparent by inspecting Fig. 3(**d**), the OER activity of NiFeP@NPC does not degrade significantly over 2000 cycles. Also, from the inset of Fig. 3(**d**) the potential required to deliver a current density of 10 mA cm^{-2} does not change significantly (increased by 0.02 V) after 20 h, suggesting good catalytic durability. As shown in **Fig. S10** (**a**) and (**b**), the tube morphology of NiFeP@NPC does not appear to be affected by the chronopotentiometric tests, and the NiFeP nanoparticles remain well embedded in the graphitic layers, supporting its good stability. In addition, XPS of NiFeP@NPC after the chronopotentiometric test is also collected. From **Fig. S10**(**c**) and (**d**), positive shifts to higher binding energy regions are detected for Ni 2p and Fe 2p in comparison to those in pristine NiFeP@NPC, suggesting Ni and Fe are partially oxidized on the surface under OER chronopotentiometric test. This kind of partial oxidation for TMPs during OER has been reported before [19,21]. Those oxidized moieties are likely be transition metal oxides/hydroxides, which are believed to be active species for OER electrocatalysis [35,65].

The ECSA is proportional to the electrochemical double-layer capacitance C_{DL}, which is obtained by scanning CVs between 1.1 and 1.2 V vs. RHE, a potential region where Faradaic current is small [2,43,48,49]. As shown in **Fig. S11**, NiFeP@NPC has a capacitive current greater than that of Ni_2P@NPC and NiFeP@PC. The calculated specific double layer capacitance of NiFeP@NPC (3.67 m F cm^{-2}) is approximately 1.4–2.9 times larger than that of monometallic Ni_2P@NPC (2.69 m F cm^{-2}) and NiFeP@PC (1.26 m F cm^{-2}), as shown in Fig. 4(**a**), suggesting a substantially enlarged electrochemically active area. In addition, from the EIS reported in Fig. 4(**b**) and the corresponding fitting, see **Fig. S12** and **Table S3**, NiFeP@NPC has a substantially reduced charge transfer resistance in comparison to Ni_2P@NPC and NiFeP@PC. Unlike NiFeP@PC where the carbons are disordered, the carbon tube in NiFeP@NPC and Ni_2P@NPC is favorable to provide a continuous pathway for charge transport, and improve the exchangeability between the catalyst surface and the inner layers, which can potentially extend the active sites on the surface into the internal parts, leading to a larger ECSA [43,56,62]. Moreover, in-situ synthesized bimetallic catalysts contribute to a higher degree of graphitization and a reduced disorder for carbon materials than monometal counterparts [41,43,56], supported by the lower I_D/I_G ratio in the Raman spectroscopy in Fig. 1(**b**). The reduced disorder in carbon materials is favorable to increase the electrical conductivity and reduces

the charge transfer resistance during electrocatalysis. In addition, alloying bimetals could potentially modify the electronic structure (see the XPS shift in Fig. 1(**g**) and (**h**)) and contribute to a number of additional synergistic benefits, despite the fact that the mechanism behind that is still under debate [66–68]. For example, it has been reported that Fe doping into Ni can improve the electronic conductivity of NiFe-based electrocatalysts [67], and there are also other studies demonstrating that Fe doping can induce structural transformations of Ni-based catalysts making it easier to form OER-active species [68]. In addition, combining different bimetals in TMPs may optimize the binding of OER intermediates such as OH, O, OOH, leading to faster OER kinetics [69]. Finally, we investigated the effect of two key preparation factors influencing OER activity of NiFeP@NPC, see **Fig. S13**, namely 1) the concentration of transition metals added to the precursors; and 2) the pyrolysis temperature. Increasing the mass of transition metals by a factor of 10, leads to a slightly reduced I_D/I_G ratio in the Raman spectrum (see **Fig. S13**(**a**)). However, we observe transition metal phosphide nanoparticles were agglomerated for NiFeP10@NPC (**Fig. S13**(**b**)). This kind of agglomeration will reduce the active surface area, and prevent reactants from accessing the internal parts of the electrocatalysts. Moreover, excessive amount of transition metal may potentially block the pores of the carbon, resulting in lowered BET surface area (Fig. 1(**c**)) and decreased OER activity in comparison to NiFeP@NPC (**Fig. S13**(**c**)). In addition, adjusting the pyrolysis temperature is found to influence the OER activity of the samples. For the 800 °C pyrolysis, we achieved the highest OER activity compared to the materials prepared at 900 and 1000 °C (**Fig. S13**(**d**)). From **Table S4**, the remained amounts of transition metals (Ni and Fe, ~2 at. %) are similar among the samples prepared at different temperatures. However, at 800 °C, the prepared sample has the largest BET surface area and highest heteroatom content ((N + P):C, where we subtracted the contributions from TMPs when calculating the amount of P). A large BET surface area guarantees a high dispersion of active sites, and a high heteroatom content is able to alter the electronic structure of the adjacent carbon atoms, change the charge distribution, and facilitate the adsorption of reaction intermediates, potentially facilitating the OER electrolysis [70–72].

4. Conclusions

This work reports an in-situ synthesis of NiFe bimetallic phosphide coupled with carbon tubes, by direct pyrolysis of phytic acid sodium salt hydrate, melamine, and corresponding transition metal salts. Bimetallic NiFeP@NPC is found to be more OER-active than monometallic Ni_2P@NPC and Fe_2P@NPC, metal-free NPC, as well as NiFeP@PC. In addition, NiFeP@NPC also exceeds RuO_2 in catalyzing OER, making it a promising OER catalyst. The high performance of NiFeP@
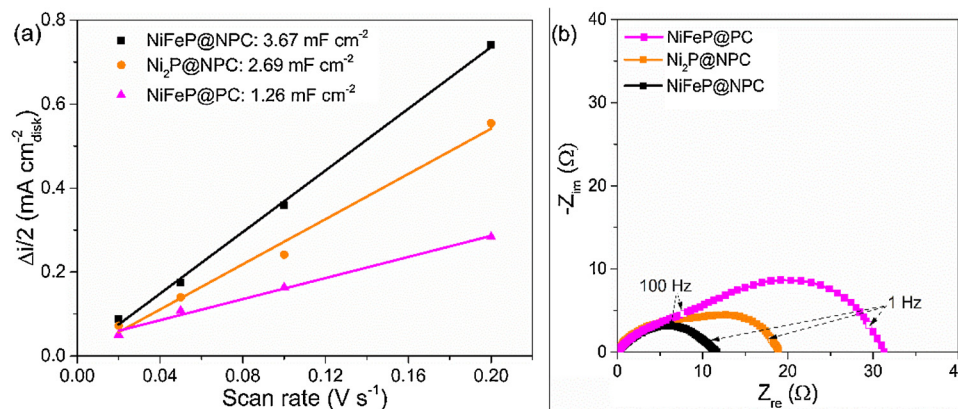

Fig. 4. (**a**) Dependence of capacitive current densities (measured at 1.15 V vs. RHE) on potential scan rates. (**b**) EIS comparison among NiFeP@NPC, Ni_2P@NPC, and NiFeP@PC.

NPC is attributed to the unique tubular structure of the carbon and the introduction of a second metal into binary TMPs, contributing to a larger electrochemical active surface area and faster charge transfer kinetics. The proposed synthesis method could provide an important reference for the preparation of other TMPs coupled with carbon tubes.

Acknowledgments

Appendix A. Supplementary data

Supplementary material related to this article can be found, in the online version, at doi:https://doi.org/10.1016/j.apcatb.2019.05.009.

References

[1] B. Zhang, X. Zheng, O. Voznyy, R. Comin, M. Bajdich, M. García-Melchor, L. Han, J. Xu, M. Liu, L. Zheng, Homogeneously dispersed multimetal oxygen-evolving catalysts, Science 352 (2016) 333–337.

[2] J. Wang, Y. Gao, D. Chen, J. Liu, Z. Zhang, Z. Shao, F. Ciucci, Water splitting with an enhanced bifunctional double perovskite, ACS Catal. 8 (2017) 364–371.

[3] D. Chen, J. Wang, Z. Zhang, Z. Shao, F. Ciucci, Boosting oxygen reduction/evolution reaction activities with layered perovskite catalysts, Chem. Commun. 52 (2016) 10739–10742.

[4] W. Zhang, K. Zhou, Ultrathin two-dimensional nanostructured materials for highly efficient water oxidation, Small 13 (2017) 1700806.

[5] M.S. Burke, L.J. Enman, A.S. Batchellor, S. Zou, S.W. Boettcher, Oxygen evolution reaction electrocatalysis on transition metal oxides and (oxy) hydroxides: activity trends and design principles, Chem. Mater. 27 (2015) 7549–7558.

[6] K. Lam, Y. Gao, J. Wang, F. Ciucci, H2O2 treated La0. 8Sr0. 2CoO3-δ as an efficient catalyst for oxygen evolution reaction, Electrochim. Acta 244 (2017) 139–145.

[7] J. Wang, Y. Gao, F. Ciucci, Mechanochemical coupling of MoS2 and perovskites for hydrogen generation, ACS Appl. Energy Mater. 1 (11) (2018) 6409–6416, https://doi.org/10.1021/acsaem.8b01365.

[8] Y. Cao, Y. Meng, S. Huang, S. He, X. Li, S. Tong, M. Wu, Nitrogen-, oxygen- and sulfur-doped carbon-encapsulated Ni3S2 and NiS Core–shell architectures: bifunctional electrocatalysts for hydrogen evolution and oxygen reduction reactions, ACS Sustain. Chem. Eng. 6 (2018) 15582–15590.

[9] Z. Pei, H. Li, Y. Huang, Q. Xue, Y. Huang, M. Zhu, Z. Wang, C. Zhi, Texturing in situ: N, S-enriched hierarchically porous carbon as a highly active reversible oxygen electrocatalyst, Energy Environ. Sci. 10 (2017) 742–749.

[10] S. Huang, Y. Meng, Y. Cao, S. He, X. Li, S. Tong, M. Wu, N-, O- and P-doped hollow carbons: metal-free bifunctional electrocatalysts for hydrogen evolution and oxygen reduction reactions, Appl. Catal. B 248 (2019) 239–248.

[11] S. Fu, C. Zhu, J. Song, M.H. Engelhard, X. Li, D. Du, Y. Lin, Highly ordered mesoporous bimetallic phosphides as efficient oxygen evolution electrocatalysts, ACS Energy Lett. 1 (2016) 792–796.

[12] D. Li, H. Baydoun, Cu.N. Verani, S.L. Brock, Efficient water oxidation using CoMnP nanoparticles, J. Am. Chem. Soc. 138 (2016) 4006–4009.

[13] M. Sun, H. Liu, J. Qu, J. Li, Earth-rich transition metal phosphide for energy conversion and storage, Adv. Energy Mater. 6 (2016) 1600087.

[14] H. Du, R.-M. Kong, X. Guo, F. Qu, J. Li, Recent progress in transition metal phosphides with enhanced electrocatalysis for hydrogen evolution, Nanoscale 10 (2018) 21617–21624.

[15] G. Zhang, G. Wang, Y. Liu, H. Liu, J. Qu, J. Li, Highly active and stable catalysts of phytic acid-derivative transition metal phosphides for full water splitting, J. Am. Chem. Soc. 138 (2016) 14686–14693.

[16] Y. Tan, H. Wang, P. Liu, Y. Shen, C. Cheng, A. Hirata, T. Fujita, Z. Tang, M. Chen, Versatile nanoporous bimetallic phosphides towards electrochemical water splitting, Energy Environ. Sci. 9 (2016) 2257–2261.

[17] P.W. Menezes, C. Panda, S. Loos, F. Bunschei-Bruns, C. Walter, M. Schwarze, X. Deng, H. Dau, M. Driess, A structurally versatile nickel phosphite acting as a robust bifunctional electrocatalyst for overall water splitting, Energy Environ. Sci. 11 (2018) 1287–1298.

[18] Y. Wang, B. Kong, D. Zhao, H. Wang, C. Selomulya, Strategies for developing transition metal phosphides as heterogeneous electrocatalysts for water splitting, Nano Today 15 (2017) 26–55.

[19] D. Li, H. Baydoun, B. Kulikowski, S.L. Brock, Boosting the catalytic performance of iron phosphide nanorods for the oxygen evolution reaction by incorporation of manganese, Chem. Mater. 29 (2017) 3048–3054.

[20] A. Mendoza-Garcia, D. Su, S. Sun, Sea urchin-like cobalt-iron phosphide as an active catalyst for oxygen evolution reaction, Nanoscale 8 (2016) 3244–3247.

[21] L. Yan, L. Cao, P. Dai, X. Gu, D. Liu, L. Li, Y. Wang, X. Zhao, Metal-organic frameworks derived nanotube of nickel–cobalt bimetal phosphides as highly efficient electrocatalysts for overall water splitting, Adv. Funct. Mater. 27 (2017) 1703455.

[22] P. Li, H.C. Zeng, Advanced oxygen evolution catalysis by bimetallic Ni–Fe phosphide nanoparticles encapsulated in nitrogen, phosphorus, and sulphur tri-doped porous carbon, Chem. Commun. 53 (2017) 6025–6028.

[23] S. Li, G. Zhang, X. Tu, J. Li, Polycrystalline CoP/CoP2 Structures for Efficient Full Water Splitting, ChemElectroChem 5 (2018) 701–707.

[24] R. Wu, D.P. Wang, K. Zhou, N. Srikanth, J. Wei, Z. Chen, Porous cobalt phosphide/graphitic carbon polyhedral hybrid composites for efficient oxygen evolution reactions, J. Mater. Chem. A 4 (2016) 13742–13745.

[25] C. Wu, Y. Yang, D. Dong, Y. Zhang, J. Li, In situ coupling of CoP polyhedrons and carbon nanotubes as highly efficient hydrogen evolution reaction electrocatalyst, Small 13 (2017) 1602873.

[26] R. Wu, D.P. Wang, X. Rui, B. Liu, K. Zhou, A.W. Law, Q. Yan, J. Wei, Z. Chen, In-situ formation of hollow hybrids composed of cobalt sulfides embedded within porous carbon polyhedra/carbon nanotubes for high-performance lithium-ion batteries, Adv. Mater 27 (2015) 3038–3044.

[27] R. Wu, D.P. Wang, K. Zhou, N. Srikanth, J. Wei, Z. Chen, Porous cobalt phosphide/graphitic carbon polyhedral hybrid composites for efficient oxygen evolution reactions, J. Mater. Chem. A 4 (2016) 13742–13745.

[28] J. Wang, H. Zhao, Y. Gao, D. Chen, C. Chen, M. Saccoccio, F. Ciucci, Ba0. 5Sr0. 5Co0. 8Fe0. 2O3 − δ on N-doped mesoporous carbon derived from organic waste as a bi-functional oxygen catalyst, Int. J. Hydrog. Energy 41 (2016) 10744–10754.

[29] W. Xiaoguang, L. Wei, X. Dehua, D.Y. Petrovykh, L. Lifeng, Bifunctional nickel phosphide nanocatalysts supported on carbon fiber paper for highly efficient and stable overall water splitting, Adv. Funct. Mater. 26 (2016) 4067–4077.

[30] C.-C. Hou, S. Cao, W.-F. Fu, Y. Chen, Ultrafine CoP nanoparticles supported on carbon nanotubes as highly active electrocatalyst for both oxygen and hydrogen evolution in basic media, ACS Appl. Mater. Inter. 7 (2015) 28412–28419.

[31] S. Wang, L. Zhang, X. Li, C. Li, R. Zhang, Y. Zhang, H. Zhu, Sponge-like nickel phosphide–carbon nanotube hybrid electrodes for efficient hydrogen evolution over a wide pH range, Nano Res. 10 (2017) 415–425.

[32] X. Zhang, X. Zhang, H. Xu, Z. Wu, H. Wang, Y. Liang, Iron-doped cobalt monophosphide nanosheet/carbon nanotube hybrids as active and stable electrocatalysts for water splitting, Adv. Funct. Mater. 27 (2017) 1606635.

[33] S. Huang, Y. Meng, S. He, A. Goswami, Q. Wu, J. Li, S. Tong, T. Asefa, M. Wu, N-, O-, and S-tridoped carbon-encapsulated Co9S8 nanomaterials: efficient bifunctional electrocatalysts for overall water splitting, Adv. Funct. Mater. 27 (2017) 1606585.

[34] H. Peilei, Y. Xin-Yao, L.X. Wen, Carbon-incorporated nickel–cobalt mixed metal phosphide nanoboxes with enhanced electrocatalytic activity for oxygen evolution, Angew. Chem. 129 (2017) 3955–3958.

[35] X.-Y. Yu, Y. Feng, B. Guan, X.W. Lou, U. Paik, Carbon coated porous nickel phosphides nanoplates for highly efficient oxygen evolution reaction, Energy Environ. Sci. 9 (2016) 1246–1250.

[36] Z. Pu, C. Zhang, I.S. Amiinu, W. Li, L. Wu, S. Mu, General strategy for the synthesis of transition-metal phosphide/N-doped carbon frameworks for hydrogen and oxygen evolution, ACS Appl. Mater. Inter. 9 (2017) 16187–16193.

[37] Z. Pu, I.S. Amiinu, C. Zhang, M. Wang, Z. Kou, S. Mu, Phytic acid-derivative transition metal phosphides encapsulated in N,P-codoped carbon: an efficient and durable hydrogen evolution electrocatalyst in a wide pH range, Nanoscale 9 (2017) 3555–3560.

[38] D.Y. Chung, S.W. Jun, G. Yoon, H. Kim, J.M. Yoo, K.-S. Lee, T. Kim, H. Shin, A.K. Sinha, S.G. Kwon, Large-scale synthesis of carbon-shell-coated FeP nanoparticles for robust hydrogen evolution reaction electrocatalyst, J. Am. Chem. Soc. 139 (2017) 6669–6674.

[39] P. Trogadas, T.F. Fuller, P. Strasser, Carbon as catalyst and support for electrochemical energy conversion, Carbon 75 (2014) 5–42.

[40] S. Gupta, L. Qiao, S. Zhao, H. Xu, Y. Lin, S.V. Devaguptapu, X. Wang, M.T. Swihart, G. Wu, Highly active and stable graphene tubes decorated with FeCoNi alloy nanoparticles via a template-free graphitization for bifunctional oxygen reduction and evolution, Adv. Energy Mater. 6 (2016).

[41] W.-Q. Deng, X. Xu, W.A. Goddard, A two-stage mechanism of bimetallic catalyzed growth of single-walled carbon nanotubes, Nano Lett. 4 (2004) 2331–2335.

[42] J. Wang, Y. Gao, T.L. You, F. Ciucci, Bimetal-decorated nanocarbon as a superior electrocatalyst for overall water splitting, J. Power Sources 401 (2018) 312–321.

[43] J. Wang, F. Ciucci, Boosting bifunctional oxygen electrolysis for N-doped carbon via bimetal addition, Small 13 (2017) 1604103.

[44] D. Das, K.K. Nanda, One-step, integrated fabrication of Co2P nanoparticles encapsulated N, P dual-doped CNTs for highly advanced total water splitting, Nano Energy 30 (2016) 303–311.

[45] W. Yang, X. Liu, X. Yue, J. Jia, S. Guo, Bamboo-like carbon nanotube/Fe3C nanoparticle hybrids and their highly efficient catalysis for oxygen reduction, J. Am. Chem. Soc. 137 (2015) 1436–1439.

[46] K.P. Singh, E.J. Bae, J.-S. Yu, Fe–P: a new class of electroactive catalyst for oxygen reduction reaction, J. Am. Chem. Soc. 137 (2015) 3165–3168.

[47] D. Zhao, J. Feng, Q. Huo, N. Melosh, G.H. Fredrickson, B.F. Chmelka, G.D. Stucky, Triblock copolymer syntheses of mesoporous silica with periodic 50 to 300 angstrom pores, Science 279 (1998) 548–552.

[48] H. Wang, H.W. Lee, Y. Deng, Z. Lu, P.C. Hsu, Y. Liu, D. Lin, Y. Cui, Bifunctional non-noble metal oxide nanoparticle electrocatalysts through lithium-induced conversion for overall water splitting, Nat. Commun. 6 (2015) 7261.

[49] B. You, N. Jiang, M. Sheng, M.W. Bhushan, Y. Sun, Hierarchically porous urchin-like Ni2P superstructures supported on nickel foam as efficient bifunctional electrocatalysts for overall water splitting, ACS Catal. 6 (2015) 714–721.

[50] Y. Meng, X. Zou, X. Huang, A. Goswami, Z. Liu, T. Asefa, Polypyrrole-derived

nitrogen and oxygen co-doped mesoporous carbons as efficient metal-free electro-catalyst for hydrazine oxidation, Adv. Mater. 26 (2014) 6510–6516.

[51] W. Yang, X. Liu, X. Yue, J. Jia, S. Guo, Bamboo-like carbon nanotube/Fe3C nano-particle hybrids and their highly efficient catalysis for oxygen reduction, J. Am. Chem. Soc. 137 (2015) 1436–1439.

[52] W. Fan, Z. Li, C. You, X. Zong, X. Tian, S. Miao, T. Shu, C. Li, S. Liao, Binary Fe, Cu-doped bamboo-like carbon nanotubes as efficient catalyst for the oxygen reduction reaction, Nano Energy 37 (2017) 187–194.

[53] C. Tai, W. Dingsheng, Z. Jiatao, C. Chuanbao, L. Yadong, Bamboo-like nitrogen-doped carbon nanotubes with co nanoparticles encapsulated at the tips: uniform and large-scale synthesis and high-performance electrocatalysts for oxygen reduc-tion, Chem. Eur. J. 21 (2015) 14022–14029.

[54] J. Zhang, L. Qu, G. Shi, J. Liu, J. Chen, L. Dai, N, P-codoped carbon networks as efficient metal-free bifunctional catalysts for oxygen reduction and hydrogen evo-lution reactions, Angew. Chem. Int. Ed. 55 (2016) 2230–2234.

[55] D. Wei, Y. Liu, Y. Wang, H. Zhang, L. Huang, G. Yu, Synthesis of N-doped graphene by chemical vapor deposition and its electrical properties, Nano Lett. 9 (2009) 1752–1758.

[56] S. Gupta, L. Qiao, S. Zhao, H. Xu, Y. Lin, S.V. Devaguptapu, X. Wang, M.T. Swihart, G. Wu, Highly active and stable graphene tubes decorated with FeCoNi alloy na-noparticles via a template-free graphitization for bifunctional oxygen reduction and evolution, Adv. Energy Mater. 6 (2016) 1601198.

[57] Y. Feng, X.-Y. Yu, U. Paik, Nickel cobalt phosphides quasi-hollow nanocubes as an efficient electrocatalyst for hydrogen evolution in alkaline solution, Chem. Commun. 52 (2016) 1633–1636.

[58] Y. Li, Y. Zhao, H. Cheng, Y. Hu, G. Shi, L. Dai, L. Qu, Nitrogen-Doped Graphene Quantum Dots with Oxygen-Rich Functional Groups, J. Am. Chem. Soc. 134 (2012) 15–18.

[59] Y. Yang, Z. Lun, G. Xia, F. Zheng, M. He, Q. Chen, Non-precious alloy encapsulated in nitrogen-doped graphene layers derived from MOFs as an active and durable hydrogen evolution reaction catalyst, Energy Environ. Sci. 8 (2015) 3563–3571.

[60] Z. Huang, C. Lv, Z. Chen, Z. Chen, F. Tian, C. Zhang, One-pot synthesis of diiron phosphide/nitrogen-doped graphene nanocomposite for effective hydrogen gen-eration, Nano Energy 12 (2015) 666–674.

[61] S. Wang, E. Iyyamperumal, A. Roy, Y. Xue, D. Yu, L. Dai, Vertically aligned BCN nanotubes as efficient metal-free electrocatalysts for the oxygen reduction reaction: a synergetic effect by co-doping with boron and nitrogen, Angew. Chem. 123 (2011) 11960–11964.

[62] Q. Liu, J. Tian, W. Cui, P. Jiang, N. Cheng, A.M. Asiri, X. Sun, Carbon nanotubes decorated with CoP nanocrystals: a highly active non-noble-metal nanohybrid electrocatalyst for hydrogen evolution, Angew. Chem. Int. Ed. 53 (2014) 6710–6714.

[63] M. Tavakkoli, M. Nosek, J. Sainio, F. Davodi, T. Kallio, P.M. Joensuu, K. Laasonen, Functionalized carbon nanotubes with Ni (II) bipyridine complexes as efficient catalysts for the alkaline oxygen evolution reaction, ACS Catal. 7 (2017) 8033–8041.

[64] F. Davodi, M. Tavakkoli, J. Lahtinen, T. Kallio, Straightforward synthesis of ni-trogen-doped carbon nanotubes as highly active bifunctional electrocatalysts for full water splitting, J. Catal. 353 (2017) 19–27.

[65] M. Ledendecker, S. Krick Calderón, C. Papp, H.-P. Steinrück, M. Antonietti, M. Shalom, The synthesis of nanostructured Ni5P4 films and their use as a non-noble bifunctional electrocatalyst for full water splitting, Angew. Chem. Int. Ed. 54 (2015) 12361–12365.

[66] D. Friebel, M.W. Louie, M. Bajdich, K.E. Sanwald, Y. Cai, A.M. Wise, M.-J. Cheng, D. Sokaras, T.-C. Weng, R. Alonso-Mori, R.C. Davis, J.R. Bargar, J.K. Nørskov, A. Nilsson, A.T. Bell, Identification of highly active Fe sites in (Ni,Fe)OOH for electrocatalytic water splitting, J. Am. Chem. Soc. 137 (2015) 1305–1313.

[67] L. Trotochaud, S.L. Young, J.K. Ranney, S.W. Boettcher, Nickel–iron oxyhydroxide oxygen-evolution electrocatalysts: the role of intentional and incidental iron in-corporation, J. Am. Chem. Soc. 136 (2014) 6744–6753.

[68] M.W. Louie, A.T. Bell, An investigation of thin-film Ni–Fe oxide catalysts for the electrochemical evolution of oxygen, J. Am. Chem. Soc. 135 (2013) 12329–12337.

[69] X. Xiao, C.-T. He, S. Zhao, J. Li, W. Lin, Z. Yuan, Q. Zhang, S. Wang, L. Dai, D. Yu, A general approach to cobalt-based homobimetallic phosphide ultrathin nanosheets for highly efficient oxygen evolution in alkaline media, Energy Environ. Sci. 10 (2017) 893–899.

[70] X. Lu, W.-L. Yim, B.H. Suryanto, C. Zhao, Electrocatalytic oxygen evolution at surface-oxidized multiwall carbon nanotubes, J. Am. Chem. Soc. 137 (2015) 2901–2907.

[71] C. Hu, L. Dai, Multifunctional carbon-based metal-free electrocatalysts for si-multaneous oxygen reduction, oxygen evolution, and hydrogen evolution, Adv. Mater. 29 (2017) 1604942 n/a.

[72] H. Wang, N. Yang, W. Li, W. Ding, K. Chen, J. Li, L. Li, J. Wang, J. Jiang, F. Jia, Z. Wei, Understanding the roles of nitrogen configurations in hydrogen evolution: trace atomic cobalt boosts the activity of planar nitrogen-doped graphene, ACS Energy Lett. 3 (2018) 1345–1352.